LETTER

doi:10.1038/nature25452

A mildly relativistic wide-angle outflow in the neutron-star merger event GW170817

K. P. Mooley[1,2,3], E. Nakar[4], K. Hotokezaka[5], G. Hallinan[3], A. Corsi[6], D. A. Frail[2], A. Horesh[7], T. Murphy[8,9], E. Lenc[8,9], D. L. Kaplan[10], K. De[3], D. Dobie[8,9,11], P. Chandra[12,13], A. Deller[14,15], O. Gottlieb[4], M. M. Kasliwal[3], S. R. Kulkarni[3], S. T. Myers[2], S. Nissanke[16], T. Piran[7], C. Lynch[8,9], V. Bhalerao[17], S. Bourke[18], K. W. Bannister[11] & L. P. Singer[19]

GW170817 was the first gravitational-wave detection of a binary neutron-star merger[1]. It was accompanied by radiation across the electromagnetic spectrum and localized[2] to the galaxy NGC 4993 at a distance of 40 megaparsecs. It has been proposed that the observed γ-ray, X-ray and radio emission is due to an ultra-relativistic jet being launched during the merger (and successfully breaking out of the surrounding material), directed away from our line of sight (off-axis)[3–6]. The presence of such a jet is predicted from models that posit neutron-star mergers as the drivers of short hard-γ-ray bursts[7,8]. Here we report that the radio light curve of GW170817 has no direct signature of the afterglow of an off-axis jet. Although we cannot completely rule out the existence of a jet directed away from the line of sight, the observed γ-ray emission could not have originated from such a jet. Instead, the radio data require the existence of a mildly relativistic wide-angle outflow moving towards us. This outflow could be the high-velocity tail of the neutron-rich material that was ejected dynamically during the merger, or a cocoon of material that breaks out when a jet launched during the merger transfers its energy to the dynamical ejecta. Because the cocoon model explains the radio light curve of GW170817, as well as the γ-ray and X-ray emission (and possibly also the ultraviolet and optical emission)[9–15], it is the model that is most consistent with the observational data. Cocoons may be a ubiquitous phenomenon produced in neutron-star mergers, giving rise to a hitherto unidentified population of radio, ultraviolet, X-ray and γ-ray transients in the local Universe.

The radio discovery[12] of GW170817 and the observations in the month after the discovery were interpreted in the framework of a classical off-axis jet, a cocoon and dynamical ejecta. We continued to observe GW170817 with the Karl G. Jansky Very Large Array (VLA), the Australia Telescope Compact Array (ATCA) and the upgraded Giant Metrewave Radio Telescope (uGMRT), which span the frequency range 0.6–18 GHz, while optical and X-ray telescopes were constrained by proximity to the Sun. Our radio detections span up to 107 days after the merger (Fig. 1, Methods). These data show a steady rise in the radio light curve and a spectrum that is consistent with optically thin synchrotron emission. A joint temporal (time, t) and spectral (frequency, ν) power-law fit to these data of the form $S \propto \nu^{\alpha} t^{\delta}$ is well described using a spectral index $\alpha = -0.6$ and a temporal index $\delta = +0.8$ (Methods). On 2017 November 18 (93 days after the merger was detected), the peak luminosity at 1.6 GHz was 2×10^{27} erg s^{-1} Hz^{-1}, insufficient for the detection of even the nearest short hard-γ-ray burst afterglow using currently available radio telescopes[16].

The (sub-luminous) γ-ray emission that was detected immediately after the gravitational-wave detection[17] must have been emitted by a relativistic outflow[14], but an on-axis jet (scenario A in Fig. 2) was ruled out as a result of the late turn-on of the X-ray and radio emission[3–6,11–13]. If GW170817 produced a standard (luminous) short hard-γ-ray burst pointing away from us, then the interaction between the jet and the circum-merger medium would have decelerated the jet, and the afterglow emission would have eventually entered our line of sight, thus producing a so-called off-axis afterglow[18,19]. For this geometry, the light curve rises sharply and peaks when the Lorentz factor of the jet γ is approximately $1/(\theta_{\rm obs} - \theta_{\rm j})$, and then undergoes a power-law decline ($\theta_{\rm obs}$ is the angle between the axis of the jet and the line of sight and $\theta_{\rm j}$ is the opening angle of the jet). This behaviour is clearly inconsistent with the full light curve shown in Fig. 1. The rise is less steep than it would be for an off-axis jet, instead being consistent with a monotonic increase without either a plateau or a subsequent decay. Initial off-axis models (based on available X-ray and radio data at the time) predicted a radio flux density[3–5,12] of around 10 μJy (between 3 GHz and 10 GHz) approximately 100 days after the merger, whereas our measured values are at least a factor of five larger. The discrepancy with the off-axis-jet model is further demonstrated in Fig. 3, in which various jet and medium parameters are considered, showing in all cases a similar general light-curve shape that cannot fit the data. We have considered a wide range in the phase space of off-axis-jet models, and can rule out an off-axis jet (scenario B in Fig. 2) as the origin of the radio afterglow of GW170817. Even if we consider a 'structured jet', in which the outflow has an angular dependence of the Lorentz factor and energy (scenario E in Fig. 2 represents one such configuration), the observed radiation arises predominantly from a mildly relativistic outflow moving towards us (at an angle smaller than $1/\gamma$; see below), and we do not detect the observational signature of a relativistic core within the structured jet.

Having ruled out a highly collimated off-axis jet, we next consider spherical or quasi-spherical ejecta components. A single spherical shell of expanding ejecta will produce a light curve that rises as $S \propto t^3$. From the light curve of GW170817 we can immediately rule out such a simple single-velocity ejecta model. The gradual but monotonic rise seen in our radio data ($S \propto t^{0.8}$; Fig. 1) points instead to on-axis emission from a mildly relativistic blast wave in which the energy is

[1]Denys Wilkinson Building, Keble Road, Oxford OX1 3RH, UK. [2]National Radio Astronomy Observatory, Socorro, New Mexico 87801, USA. [3]California Institute of Technology, 1200 East California Boulevard, MC 249-17, Pasadena, California 91125, USA. [4]The Raymond and Beverly Sackler School of Physics and Astronomy, Tel Aviv University, Tel Aviv 69978, Israel. [5]Department Astrophysical Sciences, Princeton University, Peyton Hall, Princeton, New Jersey 08544, USA. [6]Department of Physics and Astronomy, Texas Tech University, Box 41051, Lubbock, Texas 79409-1051, USA. [7]Racah Institute of Physics, The Hebrew University of Jerusalem, Jerusalem 91904, Israel. [8]Sydney Institute for Astronomy, School of Physics, University of Sydney, Sydney, New South Wales 2006, Australia. [9]ARC Centre of Excellence for All-sky Astrophysics (CAASTRO), Australia. [10]Department of Physics, University of Wisconsin - Milwaukee, Milwaukee, Wisconsin 53201, USA. [11]ATNF, CSIRO Astronomy and Space Science, PO Box 76, Epping, New South Wales 1710, Australia. [12]National Centre for Radio Astrophysics, Tata Institute of Fundamental Research, Pune University Campus, Ganeshkhind Pune 411007, India. [13]Department of Astronomy, Stockholm University, AlbaNova, SE-106 91 Stockholm, Sweden. [14]Centre for Astrophysics and Supercomputing, Swinburne University of Technology, John Street, Hawthorn, Victoria 3122, Australia. [15]ARC Centre of Excellence for Gravitational Wave Discovery (OzGrav), Australia. [16]Institute of Mathematics, Astrophysics and Particle Physics, Radboud University, Heyendaalseweg 135, 6525 AJ Nijmegen, The Netherlands. [17]Department of Physics, Indian Institute of Technology Bombay, Mumbai 400076, India. [18]Department of Space, Earth and Environment, Chalmers University of Technology, Onsala Space Observatory, S-439 92 Onsala, Sweden. [19]Astroparticle Physics Laboratory, NASA Goddard Space Flight Center, Mail Code 661, Greenbelt, Maryland 20771, USA.

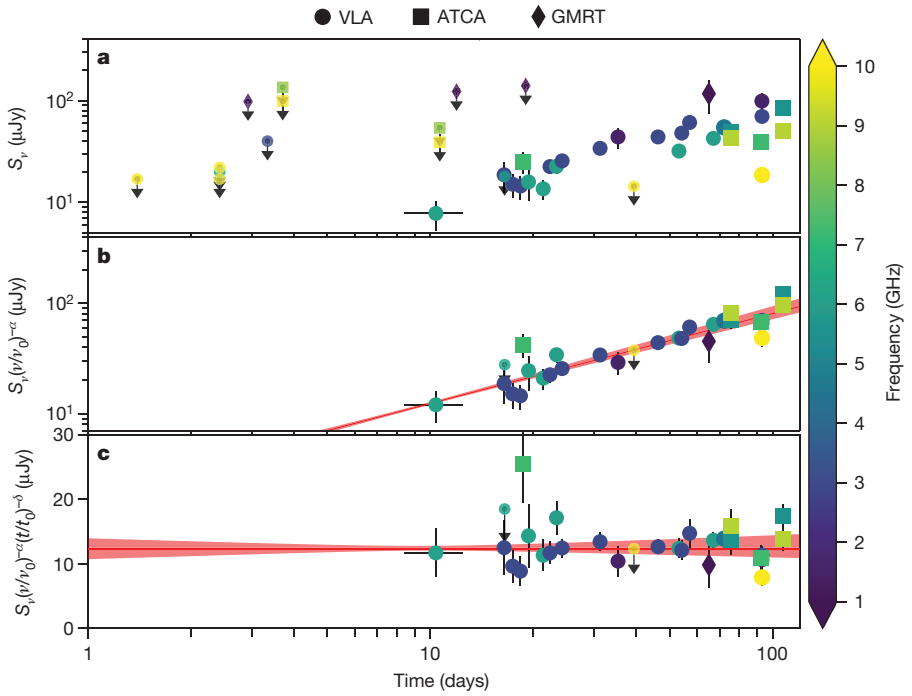

Figure 1 | The radio light curve of GW170817. **a**, The flux densities S_ν correspond to the detections (markers with 1σ error bars; some data points have errors smaller than the size of the marker) and upper limits (markers with downward-pointing arrows) of GW170817 at observing frequencies ranging from 0.6 GHz to 15 GHz (colour scale; black for $\leq$1 GHz and yellow for $\geq$10 GHz) between day 16 and day 107 after the merger. Radio data are from ref. 12 or Extended Data Table 1. The marker shapes denote measurements from different telescopes. **b**, Same as **a**, but with flux densities corrected for the spectral index $\alpha = -0.61$ (Methods) and with early-time, non-constraining upper limits removed. The fit to the light curve with temporal index $\delta = 0.78$ (Methods) is shown as a red line and the uncertainty in δ (± 0.05) as the red shaded region. **c**, Residual plot after correcting for the spectral and temporal variations (t_0 and ν_0 are normalizing parameters for the fit).

increasing with time (owing to more mass residing in slower ejecta, which is seen at later times). For example, using canonical micro-physical parameters ($\varepsilon_B = 0.01$ and $\varepsilon_e = 0.1$, the fractions of internal energy that go to the magnetic field and to the electrons, respectively), a circum-merger density of 10^{-4} cm^{-3} implies that between day 16 and day 107 after the merger, the blast wave decelerated from $\gamma \approx 3.5$ to $\gamma \approx 2.5$ and its isotropic equivalent energy increased from roughly 10^{49} erg to 10^{50} erg. On the other hand, a density of 0.01 cm^{-3} implies

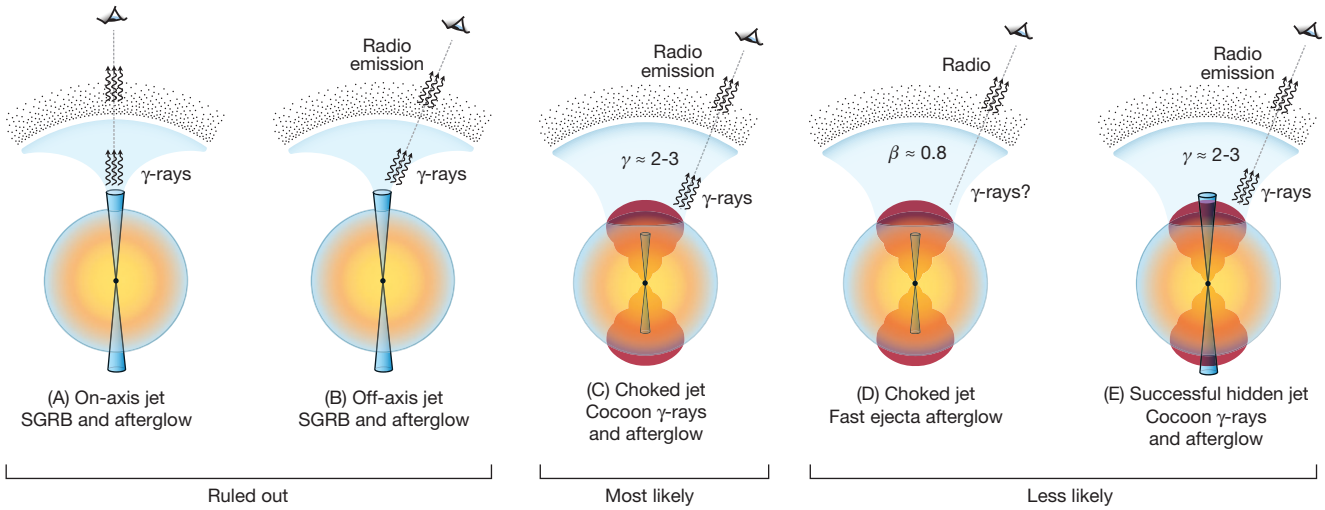

Figure 2 | Schematic of the various possible jet and dynamical ejecta scenarios in GW170817. In all cases, the black point represents the merger remnant that releases bi-conical jets, and is surrounded by the dynamical ejecta (colour-graded region); the black dotted region represents the circum-merger environment and the blue shaded region denotes the jet propagating into this environment. (A) A jet, seen on-axis, generates both the low-luminosity γ-ray emission (SGRB, short hard-γ-ray burst) and the observed radio afterglow. This scenario cannot explain the late rise of the radio emission. It is also unable to explain[11] how a low-luminosity jet penetrates the ejecta. It is therefore ruled out. (B) A standard (luminous) short hard-γ-ray burst jet, seen off-axis, produces γ-ray and radio emission. The continuous moderate rise in the radio light curve rules out this scenario. (C) A choked jet gives rise to a mildly relativistic ($\gamma \approx 2$–3) cocoon, denoted by the red shaded region, which generates the γ-rays and radio waves via on-axis emission. This is the model that is most consistent with the observational data. It accounts for the observed γ-ray and X-ray emission (and possibly also the ultraviolet and optical emission) as well as the radio emission, and provides a natural explanation for the lack of any signatures of an off-axis jet in the radio emission. (D) The high-velocity tail ($\beta \approx 0.8$–0.6, that is, $\gamma \approx 1.67$–1.25) of the ejecta produces the radio emission. In this case, the jet must be choked (otherwise its off-axis emission should have been seen). Although the radio emission is fully consistent with this scenario, the energy deposited in faster ejecta ($\gamma \approx 2$–3) must be very low. In this scenario, the source of the observed γ-ray emission remains unclear. (E) A successful jet drives a cocoon but does not have a clear signature in the radio emission. The cocoon generates the γ-ray and radio emission, and outshines the jet at all wavelengths. This scenario is less likely on the basis of theoretical considerations, which suggest that the jet and the cocoon should have comparable energies, in which case the signature of the jet would have been observed in the radio band. This scenario can also be visualized as a 'structured' jet, with a relativistic narrow core surrounded by a mildly relativistic wide-angle outflow, in which no signature of the core can be seen by an off-axis observer. The relativistic core could have produced a standard short hard-γ-ray burst for an observer located along the axis of the jet. Such a jet, if it exists, could be too weak (made a sub-dominant contribution to the radio light curve early on) or too strong (such that its radio and X-ray signatures will be observed in the future; see Methods).

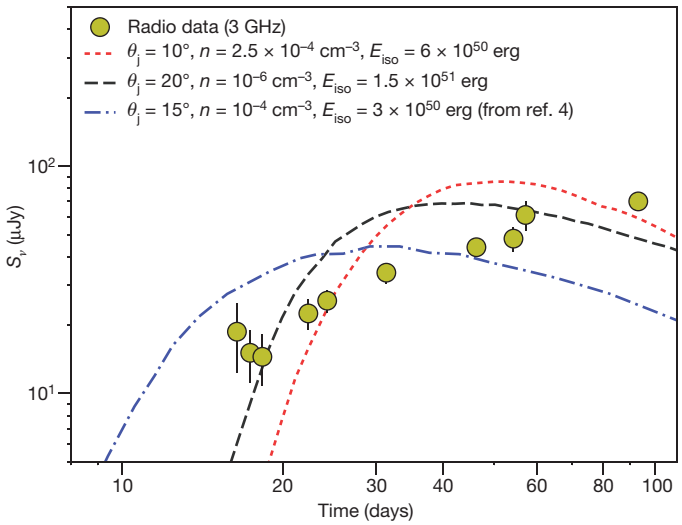

Figure 3 | Off-axis jet models. Synthetic light curves with a range of jet opening angles θ_j, isotropic-equivalent energies E_{iso} and interstellar-medium densities n (see Methods), over-plotted on the 3-GHz light curve (radio data are from ref. 12 or Extended Data Table 1; error bars are 1σ). The overall shape of the light curve remains unchanged even after changing these parameters. We have considered a wide range of parameters in the phase space of off-axis-jet models (including unlikely scenarios such as $n = 10^{-6}$ cm^{-3}; see Methods); none of the models gives a good fit to the observational data, and so we rule out the classical off-axis-jet scenario as a viable explanation for the radio afterglow. The dashed black and dotted red curves are calculated using the codes described in Methods. The dash-dotted blue curve is taken from figure 3 of ref. 4 (scaled to 3 GHz using $\alpha = -0.6$). All off-axis-jet models assume $\theta_{obs} = 26°$, $\varepsilon_e = 0.1$, $\varepsilon_B = 0.01$ and a power-law index for the non-thermal population of $p = 2.2$ (see main text and Methods).

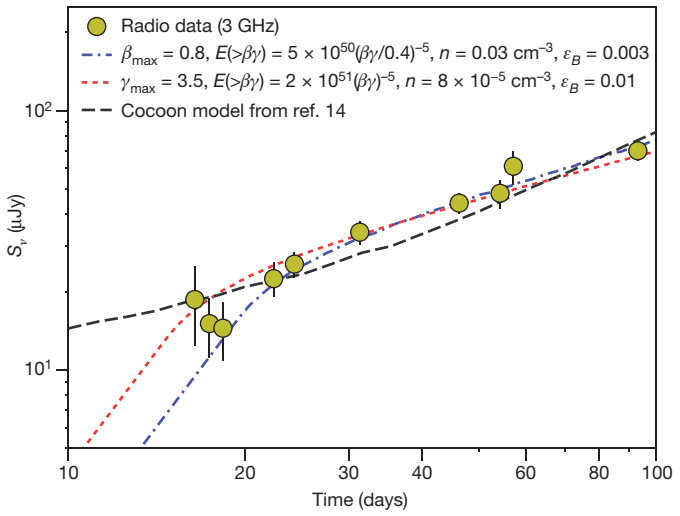

Figure 4 | Quasi-spherical ejecta models. Radio light curves arising from quasi-spherical ejecta with velocity gradients, over-plotted on the 3-GHz data for days 16–93 after the merger (radio data are from ref. 12 or Extended Data Table 1; error bars are 1σ). The solid red and dashed blue curves represent power-law models with maximum Lorentz factors of $\gamma_{max} = 3.5$ and $\gamma_{max} = 1.67$, respectively (that is, $\beta_{max} = 0.96$ and 0.8, respectively). These curves approximately correspond to the cocoon and dynamical ejecta, respectively. The shallow rise of the radio light curve is consistent with a profile $E(>\beta\gamma) \propto (\beta\gamma)^{-5}$. For $n \approx 0.03$ cm^{-3} (blue), the observed radio emission at 93 days is produced by an ejecta component with a velocity of around 0.6c and kinetic energy of around 10^{49} erg. For a lower-density interstellar medium (8×10^{-5} cm^{-3}, red), the radio emission at 93 days is produced by a component with a velocity of 0.9c and energy of 10^{50} erg. Parameters $\varepsilon_e = 0.1$ and $p = 2.2$ are used for both models. The cocoon-model light curve[14] (dotted black curve) is also shown for reference, with parameter values of $n = 1.3 \times 10^{-4}$ cm^{-3}, $\varepsilon_B = 0.01$, $\varepsilon_e = 0.1$ and $p = 2.1$.

a velocity range of 0.8c to 0.65c (where c is the light speed) and an energy that increases from 10^{48} erg to 10^{49} erg. Figure 4 demonstrates that a quasi-spherical outflow with a velocity profile described by $E(>\beta\gamma) \propto (\beta\gamma)^{-5}$ (where β is the velocity of the ejecta in units of c and $E(>\beta\gamma)$ is the energy of the component of the ejecta with velocity greater than $\beta\gamma$), provides an excellent fit to the data (Methods), and that this profile is almost independent of the assumed circum-merger density and microphysical parameters. The energy injection into the blast wave during the time span of the observations (day 16 to day 107) increases by a factor of around 10. The possible origin of the outflow depends on the energy and velocity of the outflow. A faster and more energetic outflow, with $\gamma \approx 2$–3 and an energy of 10^{49}–10^{50} erg, is a natural outcome of a cocoon driven by a wide-angle choked jet[9,11,14] (scenario C in Fig. 2). This scenario explains many of the puzzling characteristics of GW170817. First, the breakout of a cocoon from the ejecta could produce the observed sub-luminous γ-ray signal, including its peak energy and spectral evolution[14] (see also Methods). Second, a fast and energetic outflow provides a natural explanation for the high velocities of the bulk of the ejecta (about 0.3c) and for the early bright ultraviolet and optical light[11,13,15]. On the other hand, a slower and less energetic outflow, with $\beta \approx 0.8$–0.6 ($\gamma \approx 1.67$–1.25) and an energy of 10^{48}–10^{49} erg, could arise from the fast tail of the ejecta from the merger[20–22] (scenario D in Fig. 2), although such an outflow cannot explain the γ-ray signal (GRB 170817A) from GW170817. These two scenarios can easily be distinguished by using very-long-baseline interferometry or by monitoring the radio evolution on a timescale of years.

A hidden jet, which does not contribute substantially to the observed afterglow, may still exist (scenario E in Fig. 2), but its properties are tightly constrained. First, its edge must be far enough from the line of sight (more than about 10°), which rules out off-axis γ-ray emission as the source of GRB 170817A. Second, for every reasonable set of parameters, an off-axis jet would have been brighter than the fast tail of the ejecta, implying that the observed emission must have been dominated by an outflow with $\gamma \approx 2$–3 (that is, a cocoon) for the jet to have remained undetected. In addition, the jet energy should (probably) be much lower than that of the cocoon, which is the case only for a very narrow range of jet parameters (Methods). We therefore conclude from the lack of a signature from an off-axis jet that the jet was probably choked (scenario C in Fig. 2).

We compared the 3-GHz radio and X-ray[4–6] detections obtained on 2017 September 2–3 (15–16 days after the merger was detected). The measurements at these two disparate frequencies imply a spectral index of −0.6, consistent with our multi-epoch, multi-frequency, radio-only measurements (Methods, Extended Data Fig. 4). It is therefore likely that the radio and X-rays originate from the same (synchrotron) source—a mildly relativistic outflow. This common origin can be confirmed if the X-ray flux continues to rise in a similar manner to the radio flux. We note that, although at early times the cooling break will lie well above the soft-X-ray frequencies, beyond around 100–1,000 days after the merger this break may be seen moving downwards in frequency within the electromagnetic spectrum. If the cooling break stays above 10^{18} Hz, the common origin of the radio and X-ray emission means that the Chandra telescope should detect a brighter X-ray source (flux of $(0.7–5.2) \times 10^{-14}$ erg cm^{-2} s^{-1} in the 0.3–10-keV band; see Methods) during its observation of GW170817 on 2017 December 3–6. (Subsequent to the submission of this paper, X-ray observations took place and confirmed this prediction.) If a spectral index is derived from these X-ray observations, or from observations at any time within about 1,000 days of the detection of the merger, that is different from the in-band radio spectral index presented here, it would indicate that the cooling break has already shifted below the X-ray band, which would favour the fast tail of the ejecta from the merger as the common source of the X-ray and radio emission (Methods).

The confirmation of a wide-angle outflow in GW170817 bodes well for searches for electromagnetic counterparts of future gravitational-wave events. Although on-axis (and slightly off-axis, $\theta_{obs} < 20°$) jets produce bright panchromatic afterglows, they represent only a small fraction (around 10%) of the gravitational-wave events (factoring in the larger detectable distance for face-on events[23]). By contrast, the emission from wide-angle cocoons[9–11] could potentially be seen in a much larger fraction of events and at virtually all wavelengths, thus increasing the probability of detecting electromagnetic counterparts. The radio emission from the cocoon especially, which evolves on timescales of weeks to months, provides a distinct signature (as opposed to the more common supernovae and active-galactic-nucleus transients) and diagnostics for observers. Specifically in the case of GW170817, continued monitoring of the radio light curve will provide an independent constraint on the circum-merger density and thereby on the properties of the blast wave that dominated the early-time radio emission.

Our radio data support the hypothesis of a choked jet giving rise to a mildly relativistic cocoon (scenario C in Fig. 2), but this is only one of the possible outcomes of neutron-star merger events (Fig. 2). In some cases, the jet may break out after depositing a fraction of its energy into the cocoon, thereby still successfully producing a short hard-γ-ray burst[11] (scenario E in Fig. 2). Indeed, a plateau in the distribution of the durations of short hard-γ-ray bursts has been highlighted as evidence that jets from these bursts often propagate through slower-travelling ejecta before breakout and at times are choked[24]. The relative fractions of neutron-star mergers that produce a short hard-γ-ray burst or a choked jet can be probed directly via radio follow-up observations of a sample of neutron-star mergers in the upcoming LIGO–Virgo campaigns.

Online Content Methods, along with any additional Extended Data display items and Source Data, are available in the online version of the paper; references unique to these sections appear only in the online paper.

Received 28 November; accepted 11 December 2017.
Published online 20 December 2017.

1. Abbott, B. P. *et al.* GW170817: observation of gravitational waves from a binary neutron star inspiral. *Phys. Rev. Lett.* **119,** 161101 (2017).
2. Abbott, B. P. *et al.* Multi-messenger observations of a binary neutron star merger. *Astrophys. J.* **848,** L12 (2017).
3. Alexander, K. D. *et al.* The electromagnetic counterpart of the binary neutron star merger LIGO/Virgo GW170817. VI. Radio constraints on a relativistic jet and predictions for late-time emission from the kilonova ejecta. *Astrophys. J.* **848,** L21 (2017).
4. Margutti, R. *et al.* The electromagnetic counterpart of the binary neutron star merger LIGO/Virgo GW170817. V. Rising X-ray emission from an off-axis jet. *Astrophys. J.* **848,** L20 (2017).
5. Troja, E. *et al.* The X-ray counterpart to the gravitational-wave event GW170817. *Nature* **551,** 71–74 (2017).
6. Haggard, D. *et al.* A deep Chandra X-ray study of neutron star coalescence GW170817. *Astrophys. J.* **848,** L25 (2017).
7. Eichler, D., Livio, M., Piran, T. & Schramm, D. N. Nucleosynthesis, neutrino bursts and γ-rays from coalescing neutron stars. *Nature* **340,** 126–128 (1989).
8. Nakar, E. Short-hard gamma-ray bursts. *Phys. Rep.* **442,** 166–236 (2007).
9. Gottlieb, O., Nakar, E. & Piran, T. The cocoon emission – an electromagnetic counterpart to gravitational waves from neutron star mergers. *Mon. Not. R. Astron. Soc.* **473,** 576–584 (2018).
10. Lazzati, D., Deich, A., Morsony, B. J. & Workman, J. C. Off-axis emission of short γ-ray bursts and the detectability of electromagnetic counterparts of gravitational-wave-detected binary mergers. *Mon. Not. R. Astron. Soc.* **471,** 1652–1661 (2017).
11. Kasliwal, M. M. *et al.* Illuminating gravitational waves: a concordant picture of photons from a neutron star merger. *Science* **358,** 1559–1565 (2017).
12. Hallinan, G. *et al.* A radio counterpart to a neutron star merger. *Science* **358,** 1579–1583 (2017).
13. Evans, P. A. *et al.* Swift and NuSTAR observations of GW170817: detection of a blue kilonova. *Science* **358,** 1565–1570 (2017).
14. Gottlieb, O., Nakar, E., Piran, T. & Hotokezaka, K. A cocoon shock breakout as the origin of the gamma-ray emission in GW170817. Preprint at https://arxiv.org/abs/1710.05896 (2017).
15. Piro, A. L. & Kollmeier, J. A. Evidence for cocoon emission from the early light curve of SSS17a. Preprint at https://arxiv.org/abs/1710.05822 (2017).
16. Fong, W., Berger, E., Margutti, R. & Zauderer, B. A. A decade of short-duration gamma-ray burst broadband afterglows: energetics, circumburst densities, and jet opening angles. *Astrophys. J.* **815,** 102 (2015).
17. Abbott, B. P. *et al.* Gravitational waves and gamma-rays from a binary neutron star merger: GW170817 and GRB 170817A. *Astrophys. J.* **848,** L13 (2017).
18. Granot, J., Panaitescu, A., Kumar, P. & Woosley, S. E. Off-axis afterglow emission from jetted gamma-ray bursts. *Astrophys. J.* **570,** L61–L64 (2002).
19. Nakar, E., Piran, T. & Granot, J. The detectability of orphan afterglows. *Astrophys. J.* **579,** 699–705 (2002).
20. Bauswein, A., Goriely, S. & Janka, H.-T. Systematics of dynamical mass ejection, nucleosynthesis, and radioactively powered electromagnetic signals from neutron-star mergers. *Astrophys. J.* **773,** 78 (2013).
21. Hotokezaka, K. *et al.* Mass ejection from the merger of binary neutron stars. *Phys. Rev. D* **87,** 024001 (2013).
22. Kyutoku, K., Ioka, K. & Shibata, M. Ultrarelativistic electromagnetic counterpart to binary neutron star mergers. *Mon. Not. R. Astron. Soc.* **437,** L6–L10 (2014).
23. Nissanke, S., Kasliwal, M. & Georgieva, A. Identifying elusive electromagnetic counterparts to gravitational wave mergers: an end-to-end simulation. *Astrophys. J.* **767,** 124 (2013).
24. Moharana, R. & Piran, T. Observational evidence for mass ejection accompanying short gamma-ray bursts. *Mon. Not. R. Astron. Soc.* **472,** L55–L59 (2017).

Acknowledgements We acknowledge the support and dedication of the staff of the National Radio Astronomy Observatory and particularly thank the VLA Director, M. McKinnon, as well as A. Mioduszewski and H. Medlin, for making the VLA campaign possible. We thank B. Griswold (NASA/GSFC) for beautiful graphic arts (Fig. 2). S.R.K. thanks M. Shull for discussions. The National Radio Astronomy Observatory is a facility of the National Science Foundation operated under cooperative agreement by Associated Universities, Inc. We thank the GMRT staff for scheduling our observations. The GMRT is run by the National Centre for Radio Astrophysics of the Tata Institute of Fundamental Research. The Australia Telescope Compact Array is part of the Australia Telescope National Facility, which is funded by the Australian Government for operation as a National Facility managed by CSIRO. K.P.M. is a Hintze Fellow and so is supported by the Hintze Centre for Astrophysical Surveys, which is funded through the Hintze Family Charitable Foundation. E.N. acknowledges the support of an ERC starting grant (GRB/SN) and an ISF grant (1277/13). G.H. acknowledges the support of NSF award AST-1654815. A.C. acknowledges support from the National Science Foundation CAREER award number 1455090 titled 'CAREER: Radio and gravitational-wave emission from the largest explosions since the Big Bang'. A.H. acknowledges support by the I-Core Program of the Planning and Budgeting Committee and the Israel Science Foundation. T.M. acknowledges the support of the Australian Research Council through grant FT150100099. Parts of this research were conducted by the Australian Research Council Centre of Excellence for All-sky Astrophysics (CAASTRO), through project number CE110001020. D.L.K. was supported by NSF grant AST-1412421. M.M.K.'s work was supported by the GROWTH (Global Relay of Observatories Watching Transients Happen) project funded by the NSF under PIRE grant number 1545949. This work is part of the research programme Innovational Research Incentives Scheme (Vernieuwingsimpuls), which is financed by the Netherlands Organization for Scientific Research through NWO VIDI grant number 639.042.612-Nissanke and NWO TOP grant number 62002444-Nissanke. P.C. acknowledges support from the Department of Science and Technology via SwarnaJayanti Fellowship awards (DST/SJF/PSA-01/2014-15). T.P. acknowledges the support of the Advanced ERC grant TReX. V.B. acknowledges the support of the Science and Engineering Research Board, Department of Science and Technology, India, for the GROWTH-India project.

Author Contributions K.P.M., E.N., K.H., G.H. and D.A.F. wrote the paper. A.C. compiled the references. A.C. and A.H. compiled Methods. D.D. and K.D. compiled the radio measurements table. K.P.M. managed the VLA observing programme and processed all of the VLA data. S.T.M., A.D. and S.B. helped to plan the VLA observations. E.N., K.H., D.L.K. and K.P.M. prepared the figures. T.M. planned and managed ATCA observations and data analysis and contributed to the manuscript text. D.L.K. helped to propose and plan the ATCA observations and contributed to the manuscript text. E.L., D.D., C.L. and K.W.B. helped with ATCA observations and data reduction. K.D. planned and managed GMRT observations and contributed to the manuscript text. K.P.M. and P.C. processed the GMRT data. V.B. helped with the GMRT observations. O.G. and E.N. provided the cocoon simulation. K.H. provided the spherical ejecta model. S.N. did the gravitational-wave and cocoon-rates analysis. S.R.K., T.P., M.M.K. and L.P.S. provided text for the paper. All co-authors discussed the results and provided comments on the manuscript.

Author Information Reprints and permissions information is available at www.nature.com/reprints. The authors declare no competing financial interests. Readers are welcome to comment on the online version of the paper. Publisher's note: Springer Nature remains neutral with regard to jurisdictional claims in published maps and institutional affiliations. Correspondence and requests for materials should be addressed to K.P.M. (kunal@astro.caltech.edu).

Reviewer Information *Nature* thanks S. Chatterjee and R. Wijers for their contribution to the peer review of this work.

METHODS

Radio data analysis. *VLA*. Radio observations of the GW170817 field were carried out with the Karl G. Jansky Very Large Array (VLA) in its B configuration, under a Director Discretionary Time (DDT) programme (VLA/17B-397). All observations were carried out with the Wideband Interferometric Digital Architecture (WIDAR) correlator in multiple bands, including the L band (nominal centre frequency of 1.5 GHz, with a bandwidth of 1 GHz), S band (nominal centre frequency of 3 GHz, with a bandwidth of 2 GHz) and C band (nominal centre frequency of 6 GHz, with a bandwidth of 4 GHz). We used QSO J1248−1959 (L band and S band) and QSO J1258−2219 (C band) as our phase-calibrator sources, and 3C 286 or 3C 147 as flux density and bandpass calibrators. The data were calibrated and flagged for radio-frequency interference (RFI) using the VLA automated calibration pipeline, which runs in the Common Astronomy Software Applications package (CASA[25]). We manually removed further RFI, wherever necessary, after calibration. Images of the observed field were formed using the CLEAN algorithm (with the 'psfmode' parameter set to Hogbom[26]), which we ran in the interactive mode. The results of our VLA follow-up campaign of GW170817 are reported in Extended Data Table 1 and the image cut-outs are shown in Extended Data Fig. 1. The flux densities were measured at the Gaia/HST position[27]. Uncertainties in the flux-density measurements denote the local root-mean-square (r.m.s.) noise. An additional 5% fractional error on the measured flux density is expected, owing to inaccuracies in the flux-density calibration. For non-detections, upper limits are calculated as three times the local r.m.s. noise in the image.

ATCA. We observed GW170817 on 2017 November 1, November 18 and December 2 using the Australia Telescope Compact Array (ATCA) under a Target of Opportunity programme (CX391). During these observations the array was in configurations 6A, 1.5C and 6C, respectively. We observed using two 2-GHz frequency bands with central frequencies of 5.5 GHz and 9.0 GHz. For both epochs, the flux scale and bandpass response were determined using the ATCA primary calibrator PKS B1934-638, and observations of QSO B1245−197 were used to calibrate the complex gains. The visibility data were reduced using the standard routines in the MIRIAD environment[28]. The calibrated visibility data were split into the separate bands (5.5 GHz and 9.0 GHz), averaged to 32-MHz channels, and imported into DIFMAP[29]. Bright-field sources were modelled separately for each band using the visibility data and a combination of point-source and Gaussian components with power-law spectra. With the field sources modelled and subtracted from the visibility data, the dominant emission in the residual image was from GW170817. Restored images for each band were generated by convolving the model components with the restoring beam, adding the residual map and then averaging to form a wide-band image. Image-based Gaussian fitting for an unresolved source was performed in the region of GW170817, leaving the flux density and source position unconstrained. The source position from the fitting agrees with the Gaia/HST position[27] of GW170817. The measured radio flux densities in the combined images are reported in Extended Data Table 1 and the image cut-outs are shown in Extended Data Fig. 1.

GMRT. We carried out observations of the GW170817 field with the upgraded Giant Metrewave Radio Telescope (uGMRT) at 700 MHz under a DDT programme (DDTB288). All observations were carried out with 400-MHz bandwidth centred at 750 MHz using the non-polar continuum interferometric mode of the GMRT Wideband Backend[30]. Pointings were centred at the location of the optical transient. 3C 286 was used as the absolute flux scale and bandpass calibrator, while phase calibration was done with the sources J1248−199 (for the 2017 September 16 observation) and 3C 283 (for all other observations). These data were calibrated and RFI-flagged using a custom-developed CASA pipeline. The data were then imaged interactively with the CASA task CLEAN, incorporating a few iterations of phase-only self-calibration by building a model for bright sources in the field with each iteration. The GMRT flux-density measurements at the Gaia/HST position[27] are reported in Extended Data Table 1, and the image cutouts are shown in Extended Data Fig. 1.

Radio data power-law fit. We carried out a least-squares fit to the assembled radio data as a function of time and frequency, using a two-dimensional power-law model:

$$S(\nu, t) = S_0(\nu/\nu_0)^{\alpha}(t/t_0)^{\delta}$$

The fit results are shown in Extended Data Fig. 2. We find good agreement for $\alpha = -0.61 \pm 0.05$, $\delta = 0.78 \pm 0.05$, $S_0 = 13.1 \pm 0.4\,\mu$Jy, $\nu_0 = 3$ GHz and $t_0 = 10$ d. The fit has $\chi^2 = 42.3$ for 44 degrees of freedom, although there are only 27 detections among the 47 data points.

Multi-epoch radio spectra. In Extended Data Fig. 3 we show the radio continuum spectra obtained at different epochs. All epochs are individually consistent with the spectral index $\alpha = -0.61$ within 1σ.

Model descriptions. *Off-axis afterglows*. The radio light curves were calculated using two independent semi-analytic codes[31,32], which are based on similar approximations. Both codes were compared to, and have been found to be largely consistent with, the light curves produced by the BOXFIT code[33]. In short, both codes approximate the jetted blast wave at any time in the source frame as a single zone-emitting region that is a part of a sphere with an opening angle θ_j. The hydrodynamics includes the shock location and velocity and the jet spreading. The hydrodynamic variables in the emitting region are set to their values immediately behind the shock. The emission from each location along the shock is calculated using standard afterglow theory[34], with the microphysics parameterized by the fraction of internal energy that goes to the electrons ε_e, the fraction of internal energy that goes to the magnetic field ε_B and the power-law index of the electron distribution. The code calculates the rest-frame emissivity at any time and any location along the shock. The specific flux observed at a given viewing angle at a given time and frequency is then found by integrating the contribution over equal-arrival-time surfaces, with a proper boost to the observer frame.

Quasi-spherical ejecta. Radio light curves that arise from quasi-spherical outflows—for example, a cocoon and the tail of the dynamical ejecta—are approximately described by a model with a single one-dimensional velocity profile: $E(>\beta\gamma) \propto (\beta\gamma)^{-k}$, where β is the velocity in units of the speed of light and γ is the Lorentz factor. The slope of the observed radio light curve is consistently explained with $k = 5$. The light curves are calculated using the same codes as for the off-axis-afterglow model. In Fig. 4, we show two cases: (1) a cocoon model, described by $E(>\beta\gamma) = 2 \times 10^{51}(\beta\gamma)^{-5}$ erg, with a maximum Lorentz factor of 3.5, $n = 8 \times 10^{-5}$ cm^{-3} and $\varepsilon_B = 0.01$, and (2) a dynamical ejecta model, described by $E(>\beta\gamma) = 5 \times 10^{50}(\beta\gamma/0.4)^{-5}$ erg, with a maximum velocity of $0.8c$, $n = 0.03$ cm^{-3} and $\varepsilon_B = 0.003$. The velocity profile of the dynamical ejecta contains a larger mass travelling faster than $0.6c$ by a factor of around 5 compared with that found in general-relativistic numerical simulations[20,21]. The small amount of mass that is ejected at these high velocities is plausible because the simulations are affected by finite resolution and artificial atmosphere. In addition, Fig. 4 shows a prediction from the full two-dimensional simulation of a choked jet and the resulting cocoon presented in ref. 9. The light curve is taken from figure 4 of ref. 14, without any attempt to fit the radio data that have been added since it was published. A more detailed publication reporting the full set of two-dimensional simulations is in preparation. Finally, an upper limit on the density of the interstellar medium[12] of 0.04 cm^{-3} suggests that the ejecta contains a fast-moving component with a velocity of more than about $0.6c$. For all the models shown in Fig. 4, the mass of the ejecta that produces the radio signal up to 93 days is only about 10^{-5} solar masses. This velocity is higher and the mass is much lower than those inferred from the kilonova emission[35]. We note that kilonova ejecta will produce observable radio signals on a timescale of years.

Hiding an off-axis jet. Hiding a luminous off-axis jet (of the type seen in standard short hard-γ-ray bursts), given the radio data, is not trivial. First, the jet emission peaks once its Lorentz factor drops to around $1/(\theta_{\rm obs} - \theta_j)$, where $\theta_{\rm obs}$ is the viewing angle with respect to the jet axis and θ_j is the opening angle of the jet. Therefore, emission from a jet that points only slightly away from us (less than 10°) will peak when its Lorentz factor is high (more than about 6). Because the flux in the radio band at a given time is extremely sensitive to the Lorentz factor of the blast wave (roughly as γ^{10}), a jet at that angle will be much brighter than any on-axis mildly relativistic outflow around the peak, even if the outflow carries much more energy than the jet. Therefore, a hidden jet must be far away from the line of sight, $\theta_{\rm obs} - \theta_j \gtrsim 10°$. At such angle, any γ-ray signal produced by a relativistic jet will be too faint to explain the observed γ-ray signal[11]. Thus, although our previous radio observations strongly disfavoured a standard short hard-γ-ray burst seen off-axis as the origin of the γ-rays[12] (scenario B in Fig. 2), the additional observations presented here practically rule this out.

The extreme dependence of the radio flux density on the Lorentz factor of the blast wave also implies that, for reasonable parameters also at $\theta_{\rm obs} - \theta_j \gtrsim 10°$, off-axis jet emission will outshine a blast wave driven by material with $\beta \approx 0.8$ ($\gamma \approx 1.67$). Thus, the radio emission from an off-axis jet may remain undetected only if the observed emission is dominated by an on-axis material with $\gamma \approx 3$, which is most likely to be a cocoon. In that case, a jet that is far from the line of sight may be hidden in two ways, either by being much less energetic than the on-axis outflow or, surprisingly, by being much more energetic (scenario E in Fig. 2). In the latter case the jet emission will not appear in the radio data available so far if it is so energetic that its Lorentz factor at day 93 is still much larger than $\theta_{\rm obs} - \theta_j$. For example, a 10° jet with an isotropic-equivalent energy of 10^{52} erg, which propagates in a circum-merger density of 10^{-4} cm^{-3} and is observed at an angle of 30°, peaks after 200 days and its brightness is comparable to the observed data only around day 90 ($\varepsilon_B = 0.01$, $\varepsilon_e = 0.1$). Although we cannot rule out this option, the

extreme jet energies make it unlikely; but if it is the case then we will see the jet contribution in the future.

The other possibility, that the jet is less energetic than the on-axis outflow (again scenario E in Fig. 2), cannot be tested observationally. However, it is unlikely on the basis of theoretical considerations. The energy of the cocoon is distributed over a large range of velocities. Thus, the energy of the mildly relativistic ejecta ($\gamma \approx 3$) is expected to be only a small fraction of the total cocoon energy[9]. Moreover, observationally we see that the energy carried by slower-moving on-axis material is at least a factor of 10 larger than the energy carried by high-velocity on-axis material. The ratio between the total energy in the cocoon and the energy in the jet depends on the ratio between the time spent by the jet in the ejecta before it breaks out and the time over which the jet launching continues after the breakout takes place. The engine that launches the jet is not affected by the propagation of the jet through the ejecta and is causally disconnected from the jet head, if and when it breaks out of the ejecta. Therefore, there is no reason for the engine to stop upon breakout and without fine tuning. If the jet breaks out successfully, then the launching of the jet is expected to continue over a time that is comparable to or larger than the time it takes for the jet to cross the ejecta. As a result, the energy in the jet is expected to be comparable to or larger than that in the cocoon. It is therefore highly unlikely that the jet is less energetic than the fastest cocoon material, which as noted above carries only a small fraction of the total cocoon energy.

We therefore conclude that there are no probable scenarios in which a jet successfully breaks out, producing a short hard-γ-ray burst that is seen by another (non-Earth) observer but that remains undetected by our radio observations. We find the case in which the jet is choked as the one that provides the best explanation for the entire set of observations currently available.

The origin of the γ-rays. Because a hidden jet cannot produce the observed γ-rays and the rising radio emission indicates a mildly relativistic wide-angle outflow moving towards us, we expect that this outflow is also the origin of the γ-rays. We do not see any plausible scenario in which the kilonova ejecta produces the γ-rays by itself. Compactness arguments imply that this ejecta is too slow[11,14] and that there is no natural dissipation process that could convert the kinetic energy of the ejecta to γ-rays. The cocoon, on the other hand, could produce the observed γ-rays, in the presence of a dissipation mechanism[9,10,36,37]: it has sufficient energy and its Lorentz factor is sufficiently high to avoid compactness issues. For example, a breakout of the shock driven by the cocoon through the expanding ejecta could produce the observed signal, accounting for its luminosity, duration, peak energy and spectral evolution[9].

Lower limit for the circum-merger density. The mean cosmological baryon density is a function of the ratio of deuterium to hydrogen (D/H ratio)[38], the primordial helium density[39], cosmographic parameters[40] and the fraction of diffuse baryons in the intergalactic medium ($f_{\rm IGM}$), and is given[41] as

$$n_{\rm H} \approx (1.88 \times 10^{-7}\ {\rm cm}^{-3}) f_{\rm IGM} (1+z)^3$$

where z is the redshift. We adopt[41] $f_{\rm IGM} = 0.7$. At $z \approx 0$, a density of $10^{-6}\ {\rm cm}^{-3}$ corresponds to a baryon overdensity of $\Delta_{\rm b} = 5$. For the Lyman-α forest, $\Delta_{\rm b}$ is in the range 10–50, whereas that in condensed halos[41] is in the range 10^2–10^4. Therefore, in the case of GW170817, a lower limit for the ambient density is $2 \times 10^{-5}\ {\rm cm}^{-3}$ and a typical value[42] would be roughly $10^{-4}\ {\rm cm}^{-3}$.

Radio–X-ray comparison. The 3-GHz flux density measured[12] on 2017 September 3.9 is $15 \pm 4\ \mu$Jy. By scaling the X-ray fluxes given in ref. 6 (reported in the energy range 0.3–8 keV) to the values reported in ref. 5 (0.3–10 keV), we estimate the X-ray flux on 2017 September 2.2 as $5.5 \times 10^{-15}\ {\rm erg\ cm^{-2}\ s^{-1}}$, with a 1σ uncertainty of approximately $1.5 \times 10^{-15}\ {\rm erg\ cm^{-2}\ s^{-1}}$. We use this information (X-ray flux density of 0.23 ± 0.06 nJy at a nominal centre frequency of 4×10^{17} Hz) to calculate the spectral index between the radio and X-ray frequencies as -0.60 ± 0.03. This is consistent with our estimated value of the radio-only spectral index, -0.61 ± 0.05, within 1σ. Therefore the radio emission and X-rays probably originate from the same source, and the cooling frequency around 16 days after the merger is well above the soft-X-ray frequencies. Extended Data Fig. 4 shows a panchromatic spectrum between the radio and X-ray frequencies. Ultraviolet and near-infrared data are also plotted for comparison. Although the early-time emission in the ultraviolet, optical and infrared frequencies is dominated by thermal emission, at late times there should be a substantial synchrotron component. Using the temporal and spectral indices estimated for the radio-only data (earlier in Methods), and assuming that the cooling break remains beyond 10^{18} Hz, we predict X-ray flux densities of 0.3–2.2 nJy (flux of $(7\text{–}52) \times 10^{-15}\ {\rm erg\ cm^{-2}\ s^{-1}}$ in the 0.3–10-keV band) on 2017 November 18 (and also for the Chandra observation on December 3–6). We note that, subsequent to the submission of this paper, the X-ray observations took place and confirmed our prediction. We estimate the synchrotron cooling frequency as:

$$\nu_{\rm c} \approx 7 \times 10^{19} \left(\frac{\gamma}{2}\right)^{-4} \left(\frac{n}{10^{-4}\ {\rm cm}^{-3}}\right)^{-\frac{3}{2}} \left(\frac{\varepsilon_{\rm B}}{0.01}\right)^{-\frac{3}{2}} \left(\frac{t}{100\ {\rm d}}\right)^{-2}\ {\rm Hz}$$

for $\gamma \gg 1$ (as expected for the cocoon) and

$$\nu_{\rm c} \approx 2 \times 10^{18} \left(\frac{\beta}{0.6}\right)^{-3} \left(\frac{n}{0.03\ {\rm cm}^{-3}}\right)^{-\frac{3}{2}} \left(\frac{\varepsilon_{\rm B}}{0.003}\right)^{-\frac{3}{2}} \left(\frac{t}{100\ {\rm d}}\right)^{-2}\ {\rm Hz}$$

for $\beta \ll 1$ (that is, $\gamma \approx 1$, as expected for the tail of the dynamical ejecta). We see that the cooling frequency at around day 16 after the merger is much larger than 10^{18} Hz, whereas beyond about 100–1,000 days after the merger this break should be seen moving towards lower frequencies within the electromagnetic spectrum.

Data availability. All relevant data are available from the corresponding author on request. Data presented in Fig. 1 are included in Extended Data Table 1.

Code availability. The codes used to generate the synthetic radio light curves are currently being readied for public release. We used the radio data processing software CASA, MIRIAD and DIFMAP.

25. McMullin, J. P., Waters, B., Schiebel, D., Young, W. & Golap, K. CASA architecture and applications. *ASP Conf. Ser.* **376,** 127–130 (2007).
26. Högbom, J. A. Aperture synthesis with a non-regular distribution of interferometer baselines. *Astron. Astrophys.* Suppl. **15,** 417–426 (1974).
27. Adams, S. M., Kasliwal, M. M. & Blagorodnova, N. LIGO/VIRGO G298048: precise position of SSS17a based on HST and Gaia. *GCN Circ.* 21816 (2017).
28. Sault, R. J., Teuben, P. J. & Wright, M. C. H. A retrospective view of MIRIAD. *ASP Conf. Ser.* **77,** 433–436 (1995).
29. Shepherd, M. C. Difmap: an interactive program for synthesis imaging. *ASP Conf. Ser.* **125,** 77–84 (1997)
30. Reddy, S. H. *et al.* A wideband digital back-end for the upgraded GMRT. *J. Astron. Instrum.* **6,** 1641011 (2017).
31. Soderberg, A. M., Nakar, E., Berger, E. & Kulkarni, S. R. Late-time radio observations of 68 type Ibc supernovae: strong constraints on off-axis gamma-ray bursts. *Astrophys. J.* **638,** 930–937 (2006).
32. Hotokezaka, K. & Piran, T. Mass ejection from neutron star mergers: different components and expected radio signals. *Mon. Not. R. Astron. Soc.* **450,** 1430–1440 (2015).
33. van Eerten, H. J. & MacFadyen, A. I. Observational implications of gamma-ray burst afterglow jet simulations and numerical light curve calculations. *Astrophys. J.* **751,** 155 (2012).
34. Sari, R., Piran, T. & Narayan, R. Spectra and light curves of gamma-ray burst afterglows. *Astrophys. J.* **497,** L17–L20 (1998).
35. Villar, V. A. *et al.* The combined ultraviolet, optical, and near-infrared light curves of the kilonova associated with the binary neutron star merger GW170817: homogenized data set, analytic models, and physical implications. *Astrophys. J.* **851,** L21 (2017)
36. Nakar, E. & Piran, T. The observable signatures of GRB cocoons. *Astrophys. J.* **834,** 28 (2016).
37. Lazzati, D. *et al.* Off-axis prompt X-ray transients from the cocoon of short gamma-ray bursts. *Astrophys. J.* **848,** L6 (2017).
38. Cooke, R. J., Pettini, M., Nollett, K. M. & Jorgenson, R. The primordial deuterium abundance of the most metal-poor damped Lyman-α system. *Astrophys. J.* **830,** 148 (2016).
39. Aver, E., Olive, K. A., Porter, R. L. & Skillman, E. D. The primordial helium abundance from updated emissivities. *J. Cosmol. Astropart. Phys.* **11,** 17 (2013).
40. Planck Collaboration. Planck 2015 results. XIII. Cosmological parameters. *Astron. Astrophys.* **594,** A13 (2016).
41. Shull, M. J., Smith, B. D. & Danforth, C. W. The baryon census in a multiphase intergalactic medium: 30% of the baryons may still be missing. *Astrophys. J.* **759,** 23 (2012).
42. Tumlinson, J., Peeples, M. S. & Werk, J. K. The circumgalactic medium. *Annu. Rev. Astron. Astrophys.* **55,** 389–432 (2017).

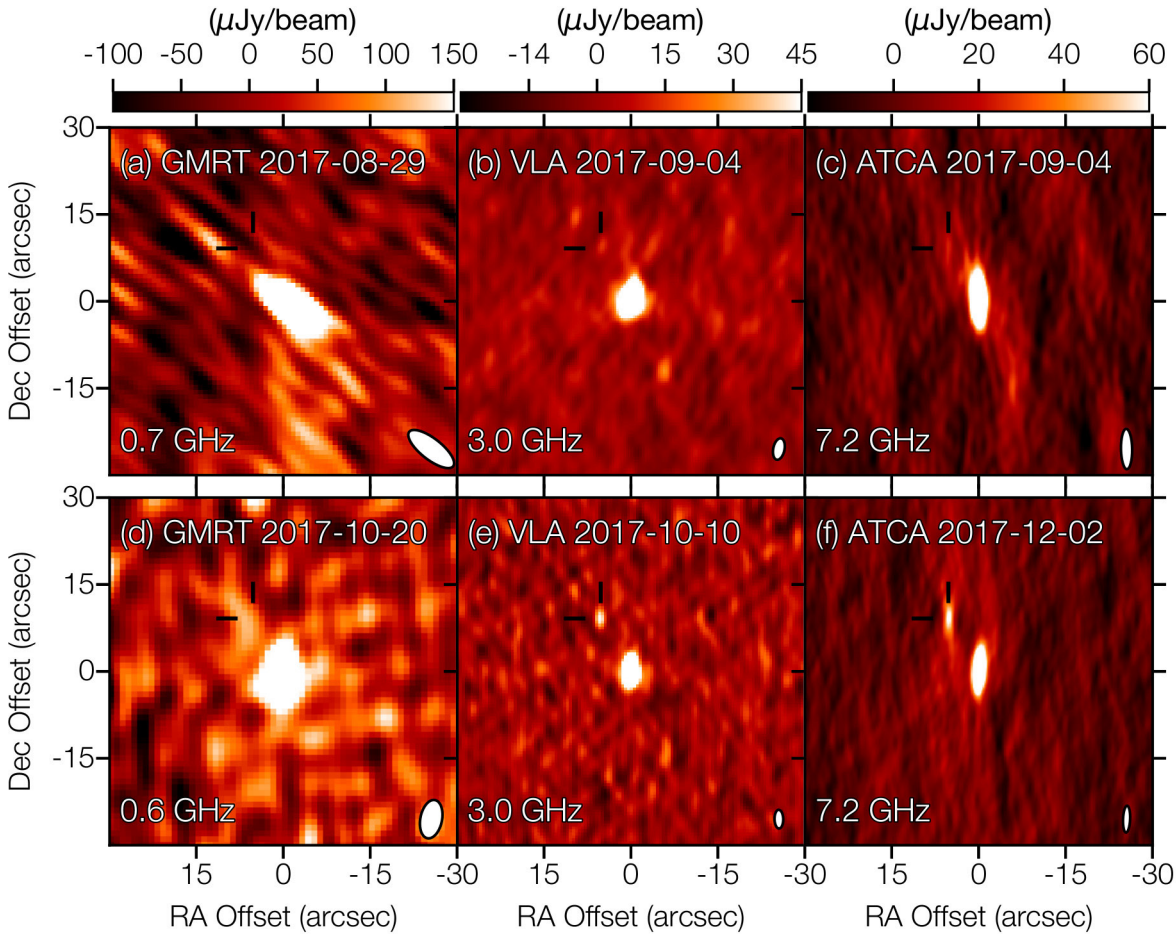

Extended Data Figure 1 | GW170817 radio image cut-outs. Image cut-outs (30″ × 30″) from uGMRT (**a**, **d**), VLA (**b**, **e**) and ATCA (**c**, **f**) are shown, centred on NGC 4993. The position of GW170817 is marked by two black lines. **a**–**c**, Images from August–September 2017, using the data reported in ref. 12. **d**–**f**, Data from October and December 2017. The flux density is indicated by the colour scale in each column. The synthesized beam is shown as an ellipse in the lower right corner of each image. Dec, declination; RA, right ascension.

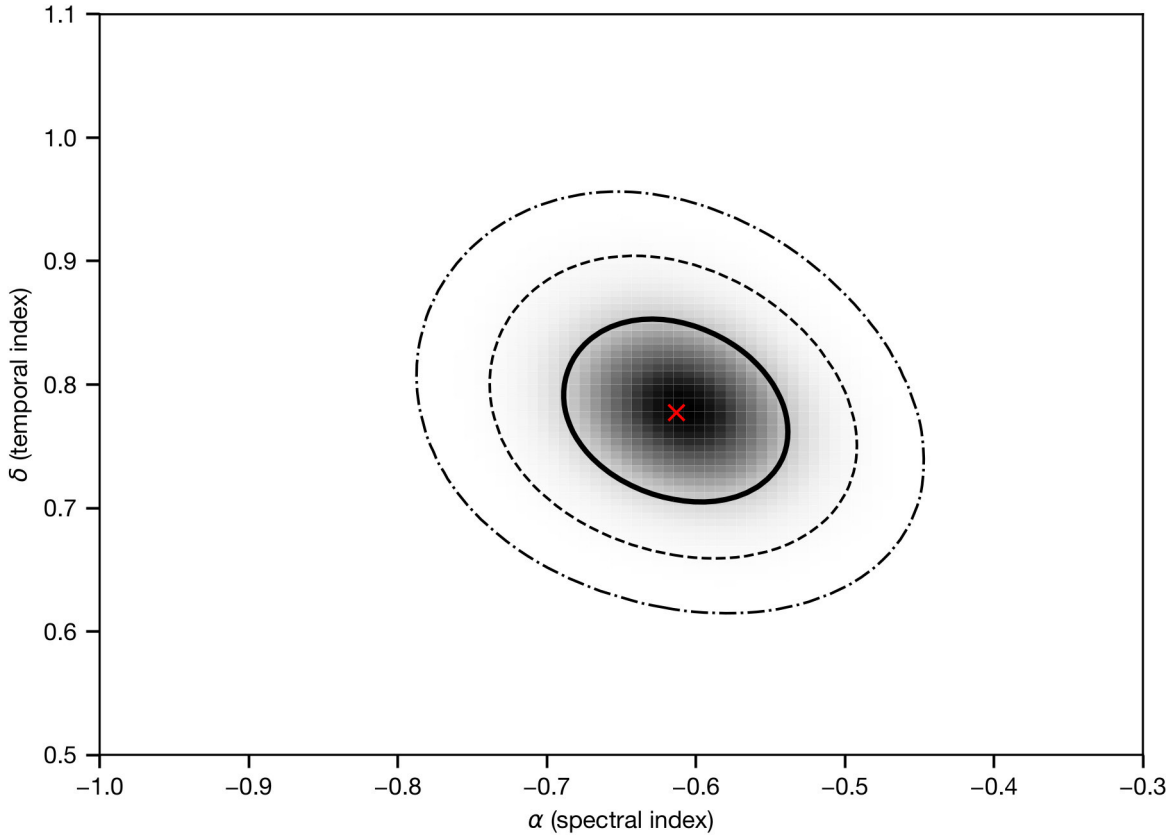

Extended Data Figure 2 | Confidence region for the radio spectral and temporal indices. Joint confidence contours for α (the spectral power-law index) and δ (the temporal power-law index) are shown. The contours are 1σ, 2σ and 3σ confidence contours, and the location of the best-fit values, $\alpha = -0.61 \pm 0.05$ and $\delta = 0.78 \pm 0.05$, is indicated by the red cross.

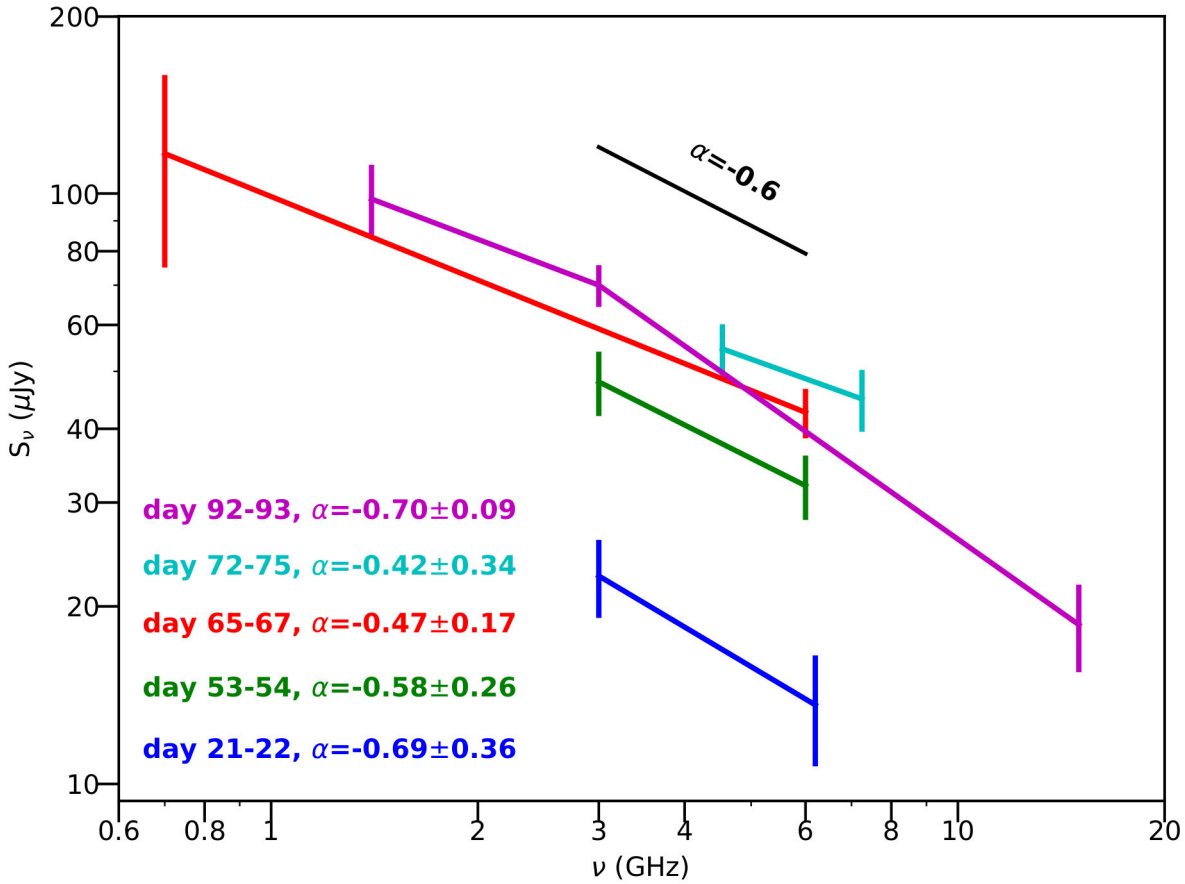

Extended Data Figure 3 | Radio-only spectral indices of GW170817. Radio spectral indices between 0.6 GHz and 15 GHz spanning multiple epochs (colour-coded) are shown. The corresponding days after the merger was detected and spectral indices are given in the legend. Error bars are 1σ. The joint analysis of all radio data (Methods) implies $\alpha = -0.61 \pm 0.05$.

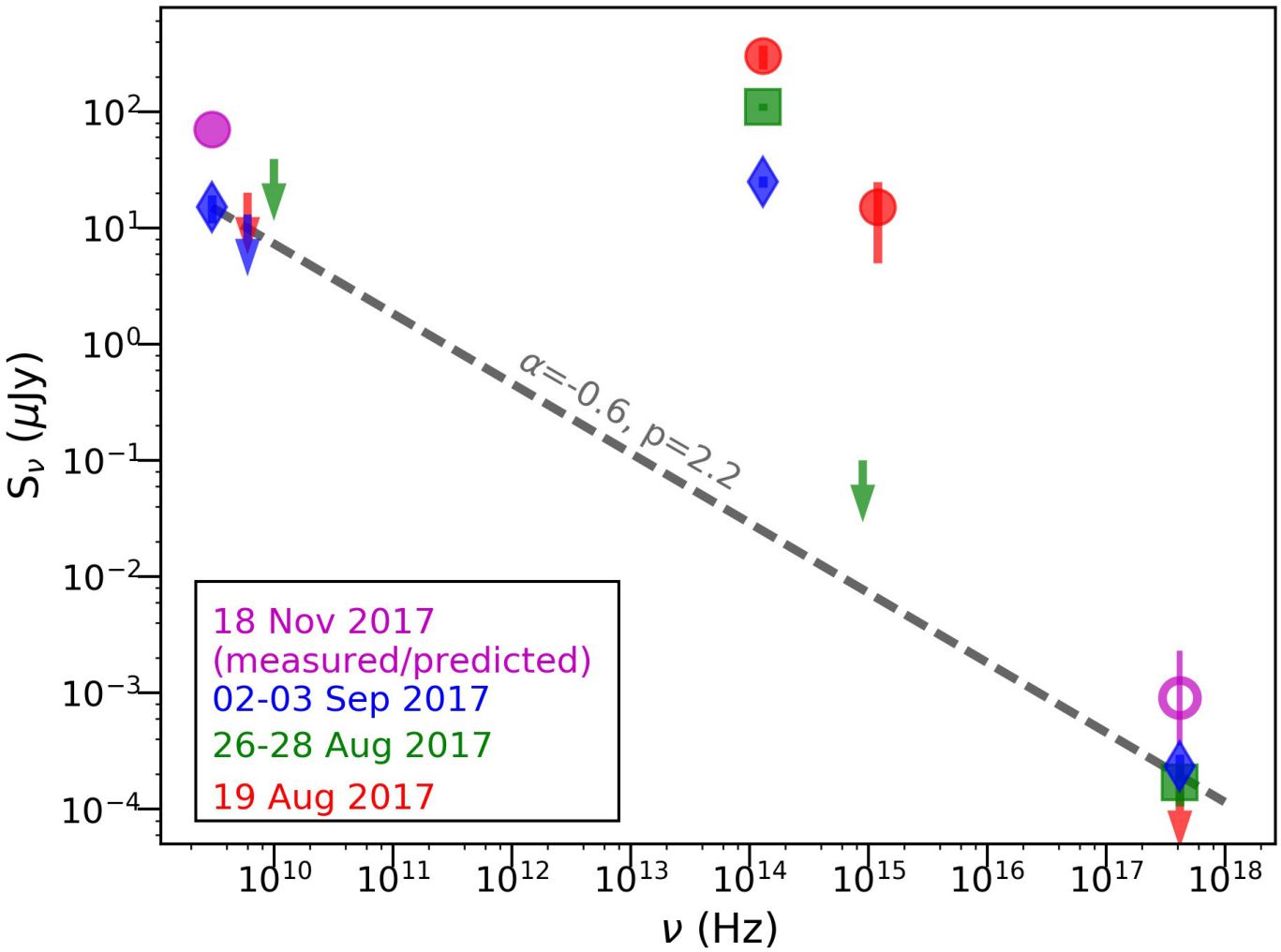

Extended Data Figure 4 | Comparison between the radio and X-ray flux densities of GW170817. The X-ray data are compared to the radio upper limits (arrows) and detections (filled symbols) at different epochs (colour-coded, see legend, and marked with different symbols). The difference epochs are 2017 August 19, August 26–28, September 2–3 and November 18 (2 days, around 10 days, around 15 days and 93 days after the merger was detected, respectively). Error bars are 1σ. The spectral index $\alpha = -0.60 \pm 0.03$ and corresponding electron power-law index $p = 2.20 \pm 0.06$ (assuming that the cooling frequency is beyond 10^{18} Hz, as expected for a mildly relativistic outflow) between 3 GHz and 10^{18} Hz, as derived from the September 2–3 data, are consistent with the radio-only spectral indices, and shown here as a dashed grey line. This indicates that the radio and X-ray emission originate from the same synchrotron source. The corresponding predicted soft-X-ray flux density on November 18 (0.3–2.2 nJy) is shown as an open magenta circle with an error bar. Note that the Chandra X-ray observations from December 3–6, reported after the submission of this paper, confirm this prediction. The flux densities in the ultraviolet (around 10^{15} Hz) and near-infrared (around 10^{14} Hz) bands, which are dominated by thermal emission at early times, are shown for reference.

Extended Data Table 1 | Radio data for GW170817

UT Date	ΔT (d)	Telescope	ν (GHz)	Bandwidth (GHz)	S_ν (μJy)
Sep 16.25	29.73	GMRT	0.68	0.2	< 246
Sep 17.84	31.32	VLA	3	2	34 ± 3.6
Sep 21.86	35.34	VLA	1.5	1	44 ± 10
Sep 25.86	39.34	VLA	15	4	<14.4
Oct 02.79	46.26	VLA	3	2	44 ± 4
Oct 09.79	53.26	VLA	6	4	32 ± 4
Oct 10.80	54.27	VLA	3	2	48 ± 6
Oct 13.75	57.22	VLA	3	2	61 ± 9
Oct 21.67	65.14	GMRT	0.61	0.4	117 ± 42
Oct 23.69	67.16	VLA	6	4	42.6 ± 4.1
Oct 28.73	72.20	VLA	4.5	0.5	54.6 ± 5.5
Nov 01.02	75.49	ATCA	7.25	4	44.9 ± 5.4
Nov 17.93	92.4	ATCA	7.25	4	39.6 ± 7
Nov 18.60	93.07	VLA	1.6	1	98 ± 14
Nov 18.66	93.13	VLA	3	2	70 ± 5.7
Nov 18.72	93.19	VLA	15	4	18.6 ± 3.1
Dec 02.89	107.36	ATCA	7.25	4	66.5 ± 5.6

ΔT represents the time after the merger was detected. The November 17.93 ATCA observation was affected by bad weather and so the uncertainty in the flux density for this observation is expected to be much larger than reported here. Uncertainties are 1σ.